



Published in final edited form as:

IEEE Trans Med Imaging. 2024 July ; 43(7): 2411–2419. doi:10.1109/TMI.2024.3357799.

A Comparison of Arterial Input Function Interpolation Methods for Patlak Plot Analysis of ^{68}Ga -PSMA-11 PET Prostate Cancer Studies

Nathaniel J. Smith, PhD,

Indiana University School of Medicine, Department of Radiology and Imaging Sciences, Indianapolis, IN.

Purdue University, Weldon School of Biomedical Engineering, West Lafayette, IN.

David T. Newton, PhD [statistician],

Purdue University, West Lafayette, IN

David Gunderman, PhD,

Indiana University School of Medicine, Lafayette, IN

Gary D. Hutchins, PhD

Indiana University School of Medicine, Department of Radiology and Imaging Sciences, Indianapolis, IN.

Abstract

Positron emission tomography (PET) imaging enables quantitative assessment of tissue physiology. Dynamic pharmacokinetic analysis of PET images requires accurate estimation of the radiotracer plasma input function to derive meaningful parameter estimates, and small discrepancies in parameter estimation can mimic subtle physiologic tissue variation. This study evaluates the impact of input function interpolation method on the accuracy of Patlak kinetic parameter estimation through simulations modeling the pharmacokinetic properties of [^{68}Ga]-PSMA-11. This study evaluated both trained and untrained methods. Although the mean kinetic parameter accuracy was similar across all interpolation models, the trained node weighting interpolation model estimated accurate kinetic parameters with reduced overall variability relative to standard linear interpolation. Trained node weighting interpolation reduced kinetic parameter estimation variance by a magnitude approximating the underlying physiologic differences between normal and diseased prostatic tissue. Overall, this analysis suggests that trained node weighting improves the reliability of Patlak kinetic parameter estimation for [^{68}Ga]-PSMA-11 PET.

Keywords

arterial input function; interpolation; Patlak analysis; tracer kinetic modeling; positron emission tomography

I. INTRODUCTION

Positron emission tomography (PET) is an imaging technique that enables the quantification of physiological processes with molecular specificity using biologically-relevant molecules labeled with positron-emitting radionuclides (radiotracers). PET studies can be performed as single (static) images in time or as temporal (dynamic) sequences that measure the pharmacokinetic characteristics of the radiotracer. A single (static) PET image provides information about the average spatial distribution of tracer throughout the image acquisition window. A dynamic PET acquisition enables the estimation of key pharmacokinetic processes, such as the tissue tracer influx, trapping, and washout rates [1].

Physiologic information can be derived from dynamic PET data using mathematical models which describe the movement of tracer between distinct, well-mixed compartments using linear rate constants. In practice, the kinetic model parameters may be estimated using a number of methods, including graphical analysis, spectral analysis, and compartmental modeling [1]. All three of these methodologies require the estimation of an arterial input function (AIF), which represents the concentration of free tracer in the patient's plasma, delivered to tissue capillary beds as a function of time. Since capillary radiotracer concentrations cannot be measured in routine PET studies, large artery concentrations are used as a surrogate.

The gold standard method of measuring the AIF requires continuous arterial sampling, which often leads to patient discomfort, risk of thrombosis, and increased personnel exposure to radiation. Alternatively, population-based or image-derived AIF estimation methods are routinely employed as non-invasive measures of the AIF [2]–[9]. The AIF may be derived from a large blood pool region, preferably the cardiac left ventricle or the aorta. For smaller vessels in limited field-of-view studies, numerous methods of partial-volume correction have been investigated [10]–[12]. However, few studies have investigated the relationship between kinetic model parameters and the method of AIF interpolation. Population-based AIF estimation methods may incorrectly approximate an individual subject's variation in time-activity curves [13]. Additionally, noise in the AIF significantly impacts the variability of kinetic parameter estimates [14], [15]. A small number of parametrized models of the AIF which account for PET image reconstruction errors have been proposed, but their accuracies have not been compared against non-parametric models [16], [17].

This study's purpose is to simulate a diverse dataset of AIF data and evaluate various novel and previously reported AIF interpolation methods (both parametric and non-parametric). Each method is assessed by its ability to accurately estimate kinetic parameters through graphical (Patlak) analysis using data simulating [^{68}Ga]-PSMA-11 kinetics in prostate cancer [18]. Prostate cancer imaging with [^{68}Ga]-PSMA-11 was selected due to its demonstrated clinical utility in the detection, staging, and treatment selection for prostate cancer patients [19]–[25]. The Patlak model kinetic parameters include K_1 , the net first-order tracer influx rate, and V_d , the distribution volume, of a region. Simulations were performed using tracer pharmacokinetics which mimic results from a previously published study in prostate cancer patients [26]. Kinetic parameters inform tissue characterization and

therapeutic decisions for prostate cancer patients, so accurate AIF estimation and subsequent kinetic parameter estimation are of clinical significance [27], [28].

II. Methods

To evaluate the effects of AIF interpolation method on Patlak kinetic parameter estimates, specifically in the context of a three parameter, two tissue compartment model, a parametrized input function simulation model was developed that mimics the shape and scale of AIFs routinely observed in PET studies.

A. Input Function Model Derivation

A list of parameters, their definitions, and constraints on their simulated values may be found in Table I. The input function is modeled as a single, uniform bolus injection, $I(t)$, with parameters describing the injected dose (D), injection time delay (T_{delay}), and dose duration (T_{inject}) in (1). Two response functions ($RF_{VP}(t)$ and $RF_{LV}(t)$) represent the mixing effects of tracer in the ventriculopulmonary (2) and left ventricular (3) systems en route to the arterial system. The bolus arterial input function (4) is therefore a convolution of the injection with each response function.

$$I(t) = \begin{cases} \frac{D}{T_{inject}} & T_{delay} \leq t \leq T_{delay} + T_{inject} \\ 0 & t < T_{delay}, t > T_{delay} + T_{inject} \end{cases} \quad (1)$$

$$RF_{VP}(t) = Ve^{-Vt} \quad (2)$$

$$RF_{LV}(t) = He^{-Ht} \quad (3)$$

$$C_{bolus}(t) = I(t) \otimes RF_{LV}(t) \otimes RF_{VP}(t) \quad (4)$$

A recirculation function (5) is also introduced as a component of the overall plasma function to account for incomplete first-pass extraction and regional tissue washout of the radiotracer (6). Additionally, the input function model allows for single first-order interchange of tracer between the plasma and red blood cell (RBC) compartments in (7). When weighted by hematocrit, the plasma and RBC function combine to represent the simulated arterial input function (8). For the simulated data, input function curves were assumed to be free of imaging-system resolution distortions. Additionally, radionuclide decay was not parametrized because the model assumes that all data are decay-corrected.

$$C_{recirculated}(t + RT_{delay}) = RF e^{-RR^*t} \otimes C_{bolus}(t) \quad (5)$$

$$C_{plasma}(t) = C_{bolus}(t) + C_{recirculated}(t) \quad (6)$$

$$C_{RBC}(t) = R_1 C_{plasma}(t) \otimes e^{-R_2 t} \quad (7)$$

$$C_{blood}(t) = Hct * C_{RBC}(t) + (1 - Hct) * C_{plasma}(t) \quad (8)$$

B. Tissue Pharmacokinetic Model

Tissue curves were derived using a two tissue compartment, three rate constant (K_1, k_2, k_3) concentration model (9) [34]. A full derivation of this model is available in the supplementary materials. The central values and distributions of the three rate constants were derived from the midpoint of prostate and lesion median values observed in an experimental study by Ringheim et al [26]. Parameter variances were likewise estimated to encompass the first and third quartiles observed in the Ringheim et al. study, which modeled a three parameter, two tissue compartment model for [^{68}Ga]-PSMA-11. AIF and TAC curves were generated at 1-second resolution through random sampling from individual parameter distribution functions. The distributions which describe these parameter simulations can be found in Table I. Combining the simulated tissue and blood curves, weighted by tissue and blood volume fractions (10), produced a volume-of-interest (VOI) tracer concentration time-activity curve. Finally, the VOI curve was temporally integrated over a simulated PET acquisition sequence to represent “image-derived” data. The simulated PET acquisition sequence included twelve ten-second frames, six thirty-second frames, five one-minute frames, and ten five-minute frames for a simulated acquisition of one hour (3600 seconds). A comparison of 10 human image-derived AIFs (clinical trial [NCT04936334](#)) with simulated datasets is shown in Fig. 1.

$$C_{issue}(t) = \frac{K_1 k_2}{k_2 + k_3} e^{-(k_2 + k_3)t} \otimes C_{plasma}(t) + \frac{K_1 k_3}{k_2 + k_3} \int_0^t C_{plasma}(\tau) d\tau \quad (9)$$

$$C_{VOI}(t) = (1 - F_{BV}) C_{issue}(t) + F_{BV} C_{blood}(t)$$

(10)

$$\overline{C_{VOI}}(t | t_1 \leq t < t_2) = \frac{1}{t_2 - t_1} \int_{t_1}^{t_2} (1 - F_{BV})C_{issue}(\tau) + F_{BV}C_{blood}(\tau)d\tau$$

(11)

C. AIF Interpolation Methods

Mathematical models for the estimation of kinetic rate constants require that the AIF is generated on a fine temporal scale (typically 1 second bins) or can be parameterized mathematically. The traditional approach is to interpolate the image-derived time-activity curves (TACs) onto a 1-second grid.

Several interpolation methods described below were evaluated in this study. All simulations were constructed in Python v3.7. Using the described blood and VOI TAC models, independent training (N=20,000) and testing (N=5,000) datasets were created for the blood, plasma, and VOI TAC models. Model parameters were randomly initialized according to Table I for each data series. Additional training and testing datasets were created by adding Poisson-distributed noise characteristics to the original datasets with a random SNR between 4 and 10. Noise was applied to the TACs before scanner window integration into temporal image frames.

Trained input function interpolation models were optimized on the training dataset to minimize the errors between the blood TAC-derived plasma function and the ground-truth plasma function.

- 1) **Linear**—Linear interpolation is a common method for extracting a TAC from an image-derived AIF. Linear interpolation requires no additional training or parameterization, and thus is easy to implement in analysis workflows. Linear interpolation was performed using the midpoint time of each scanner acquisition window.
- 2) **Linear with Curve Area Preservation**—This method is a variant of linear interpolation, but it is designed to preserve the area under the curve of the original TAC. To accomplish area preservation, adjacent scanner acquisition windows of different temporal lengths are interpolated symmetrically according to the midpoint of the smaller acquisition window. Constant-value interpolation connects the missing segment to the larger acquisition window's midpoint.
- 3) **Piecewise Fit**—This method locates the peak of the arterial input function, and performs a linear fit to the peak of the curve, followed by a biexponential fit to the tail.
- 4) **Trained Node Weighting**—This method uses a training dataset to fit an independent multivariate linear predictor of the noiseless signal for each frame sequence timepoint, as a function of the measured noisy signal at every frame in the acquisition. Once trained,

the models produce estimates of the tracer concentration at each frame sequence timepoint, which are interpolated with a cubic basis function.

5) Fully-Connected Neural Network—The fully-connected (dense) network is a trained neural network which inputs a vector of noisy frame sequence data and outputs a timeseries interpolation matching the length of the study (3600s). The fully-connected network was created in PyTorch, and applied as a sequence of two linear layers with a leaky rectified linear unit activation function [35].

6) Residual Neural Network (ResNET)—The residual neural network is a single-dimensional implementation of the deep residual neural network proposed by He et al. for image recognition [36]. This network is constructed with building blocks composed of single-dimension convolutional layers and an identity connection. The overall residual network is then composed of 10 building block layers. Batch normalization and dropout ($p=50\%$) is performed within each layer, and the leaky rectified linear unit is used as the activation function. Finally, the output is passed to a single dense layer, which reports a timeseries interpolation matching the length of the study (3600s).

D. Simulation Design and Testing

Testing was performed on all interpolation models, and the models were evaluated by their AIF interpolation accuracy, as well as their Patlak parameter estimate reliability. The Patlak K_i and V_d were estimated for each data series using the linearized formulation of the Patlak tissue equation in (12) and (13). Patlak parameters were modeled without a delay term, as input functions were assumed to be derived from nearby vessels (i.e. iliac artery). When equilibrium is achieved between the compartments, a linear fit to the final six acquisition frames enables the estimation of K_i and V_d . For each testing data series, Patlak parameters were estimated for each interpolation model with and without noise added in the plasma and tissue TACs. Additionally, a control analysis using the known plasma function was used to validate the Patlak estimation method.

$$F(t) = K_i \cdot G(t) + V_d, \text{ where:}$$

$$F(t) = \frac{c_{tissue}(t)}{c_{plasma}(t)}, G(t) = \frac{\int_0^t c_{plasma}(\tau) d\tau}{c_{plasma}(t)}$$
(12)

$$K_i = \frac{K_1 k_3}{k_2 + k_3}$$
(13)

AIF interpolation performance was assessed by the mean residual and residual standard deviation (RMSE) band comparison. Additionally, differences in area under the AIF curve were assessed by repeated measure ANOVA and Dunnett's multiple comparison test, since Patlak parameter estimation depends on accurate discrete-time tracer concentration and total accumulated tracer time-activity. Assumptions of normality and sphericity were

validated. The AIF interpolation was then processed according to the Patlak equation, and the mean residual and residual standard deviation of each curve ratio was computed. K_i and V_d estimation accuracy were assessed by their residual mean and standard deviation. Additionally, the variance of parameter estimation by each method was assessed relative to linear interpolation using a one-sided F-test.

III. Results

Fig. 2 provides a visual demonstration of the parametrized plasma function, $C_{plasma}(t)$, and the modeled image-derived AIF. Fig. 3 demonstrates the variety of AIF shapes which were simulated by the model. Because the image-derived AIF is a sparse sampling of the underlying blood function, $C_{blood}(t)$, interpolative estimation enables the estimation of the underlying plasma function. The interpolation can be divided into two phases, including an early bolus or peak phase and a tail phase. The bolus phase (first 150 seconds) is frequently sampled because the signal is rapidly variant and noisy. The tail phase follows the bolus phase, and the tail phase is characterized by a slowly varying, temporally averaged signal.

Performance of each interpolation method over the bolus phase is demonstrated in Fig. 4. The linear interpolation methods and piecewise methods displayed an undulating positive and negative bias pattern, with the maximum mean bias occurring at $t=10$ seconds and the minimum mean bias occurring at $t=21$ seconds. The mean bias shifted from positive to negative between $t=15$ and $t=16$ seconds, corresponding to a shift in concavity in the mean plasma function at the same time. The bias led to average AIF peak estimation inaccuracies of $15.7 \pm 0.5\%$, $15.7 \pm 0.5\%$, and $11.7 \pm 0.5\%$ for the linear, area-preserving linear, and piecewise fit models, respectively.

The trained node weighting, fully-connected neural network, and residual neural network models did not exhibit the same behavior, as their average AIF peak prediction errors were $1.4 \pm 0.6\%$, $0.7 \pm 0.3\%$, and $4.2 \pm 0.3\%$, respectively. Irrespective of bias, all six methods demonstrated high variability in AIF peak estimation, with peak residual standard deviation greater than 300 Bq/mL in each model – approximately 10% of the average peak concentration.

Bias and variance in the AIF tail region (Fig. 5) were less pronounced. On average, all interpolation methods estimated the signal to within a standard deviation of 10 Bq/mL ($\pm 7\%$) of the target, except for the 30-to-60 and 60-to-300 second frame sequence transitions in the area-preserving linear model. However, small but consistent overestimations in the AIF tail propagated as larger biases in the total area under the AIF curve (Table II). Only the trained node weighting and fully-connected neural network models preserved unbiased estimates of the total AIF area under the curve.

When propagated to Patlak model components ($F(t)$ and $G(t)$ of (12)), the linear, linear area preservation, and trained node weighting interpolation methods estimated the plasma-integral-to-plasma ratio ($G(t)$) within a 0.12%, 0.33%, and 0.05% error margin, respectively, compared to 4.25% for piecewise fit, 2.71% for fully-connected neural network, and 5.99% for residual neural network interpolation strategies. The trained node weighting strategy

similarly estimated the tissue- to-plasma ratio within a 0.07% error margin, whereas both linear interpolation methods maintained a 1.4% error margin. Tissue-to-plasma ratios ($F(t)$) were estimated within error margins of 5.6%, 3.4%, and 4.1% for the piecewise fit, fully-connected neural network, and residual neural network interpolation methods.

Variance in AIF estimation and Patlak model components propagated to the estimation of kinetic parameters, K_i and V_d . All six methods accurately estimated K_i and V_d within standard deviation bounds on average, regardless of noise level (Figures 6 and 7). However, the trained node weighting and residual neural network interpolation approaches enabled accurate K_i estimation while statistically improving the precision of K_i estimates, relative to the linear interpolation standard (Fig. 6).

The median relative biases and standard deviations in K_i estimates were $-0.08 \pm 5.52\%$ and $1.50 \pm 5.66\%$ for the trained node weighting and residual neural network, respectively, compared to $-1.43 \pm 6.74\%$, $-1.02 \pm 6.76\%$, $-1.80 \pm 6.95\%$, and $0.81 \pm 6.94\%$ for the linear, area-preserving linear, piecewise, and fully-connected neural network interpolation models. No interpolation method significantly improved the precision of V_d estimates from noisy data relative to linear interpolation (Fig. 7), as simulated noise led to V_d standard deviations of over 40%, regardless of the interpolation method.

The testing dataset was further stratified into simulated tissue types by K_i value, according to the reference ranges provided by [26]. Fig. 8 demonstrates the differences in K_i estimation variability and bias for lesion and normal prostate. Significant underestimation of K_i was observed in the simulated normal prostate relative to the simulated lesions was noted for all methods, except the trained node weighting method. Mean bias was -2.2% for linear interpolation in the normal prostate, compared to only -0.03% for trained node weighting.

IV. Discussion

The purpose of this study was to investigate the effects of AIF interpolation techniques on the accuracy and reliability of kinetic parameter estimates obtained through Patlak analysis for [^{68}Ga]-PSMA-11 studies in prostate cancer. Ideally, an AIF interpolant possesses the ability to approximate the nonlinear plasma function while resisting the variant effects of noise. As demonstrated with the control analyses (Figs. 6 and 7), Patlak analysis accurately estimates K_i and V_d when supported by an accurate AIF interpolation. However, inaccuracies in the late-scan interpolation and area under the AIF curve estimation propagate to reduced reliability in kinetic parameter estimates.

Linear interpolant models are easy to implement and they closely adhere to the measured data from a scanner frame sequence. However, they are unable to capture underlying variations in the concavity of the AIF. As demonstrated in Fig. 4 and Table II, this manifests through bias in the estimation of the AIF peak, leading to eventual inaccuracies in the cumulative area under the curve and high K_i parameter estimation uncertainty.

In contrast to linear interpolants, model-based interpolants possess the ability to synthesize information across multiple timepoints and estimate the AIF with greater accuracy.

However, they are limited by the requirement for training datasets which must be externally validated. The trained node weighting interpolant leveraged accurate AIF peak and tail estimation to produce kinetic parameter estimates with statistically reduced variability. In contrast, although the fully-connected neural network plasma curve interpolant preserved area under the curve, it failed to converge fully in the tail region. This lack of convergence, when applied to Patlak analysis, broadened the variability of kinetic parameter estimates using the fully-connected neural network interpolant. An accurate Patlak assessment depends upon a strong tail convergence and accurate estimation of the area under the plasma curve.

The net influx rate, K_i , is estimated using a linear regression to the Patlak model formulation (12). This regression estimates the slope (K_i) through six late-timepoint frames, averaging the noise characteristics. Fig. 6 suggests that variation in the net influx rate is largely systematic, not noise-dependent. Therefore, variance in K_i estimates can be reduced by choosing accurate interpolation methods. In contrast, Fig. 7 indicates that the distribution volume (V_d) variance is highly noise-dependent, and the V_d estimation reliability improvement attributable to interpolation is only apparent when noise is removed.

In this analysis, the trained node weighting interpolant was the only method which preserved the area under the AIF plasma curve, supported accurate kinetic parameter estimates, and enabled reduced parameter estimate variability relative to standard linear interpolation. Overall, the trained node weighting method improved the accuracy of parameter estimates by 1.37%, relative to standard linear interpolation. Additionally, trained node weighting interpolation reduced the K_i estimate interquartile range by 1.45%. The residual standard deviation was also reduced 19% using the trained node weighting method.

Ringheim et al. provided the initial estimates of K_i and V_d for $[^{68}\text{Ga}]\text{-PSMA-11}$ which enabled this study. In their analysis, the lower confidence band for lesion net influx ($K_i = 0.024$) and the upper confidence band for normal prostate ($K_i = 0.022$) are only separated by a $0.002 \text{ mL}_{\text{blood}}/(\text{mL}_{\text{tissue}} \times \text{min})$ difference (9.1% relative difference) [26].

When using tracer uptake rate constants such as K_i as a metric for tissue characterization, systematic biases can lead to unnecessary false positive or negative results. Fig. 8 demonstrated significant uptake underestimation by linear interpolants in normal prostate tissue. A potential mechanism for this underestimation may involve AIF overestimation and an extension of normalized Patlak time. The K_i estimation differences seen in normal prostate and lesion are significant because the 2% bias seen in estimation with linear interpolation is of a scale which could reasonably reclassify a tissue from normal prostate to indeterminate, or indeterminate to lesion. Additionally, the tendency of linear interpolation to underestimate K_i at low values presents concern for the potential of false negative evaluations.

The reported AIF estimation methods can be applied to region-of-interest based analysis and parametric tissue modeling. Improvements in AIF estimation bias and variance become cumulatively more impactful as additional input function curves are estimated. In the context of tissue differentiation, kinetic parameters must be estimated accurately and reliably from

the most robust system available. Systematic AIF bias and variance, even if small in comparison to image noise characteristics, is a reducible error source which impacts the clinical utility of ^{68}Ga -PSMA-11 PET imaging. In this study, the trained node weighting interpolant provided the best method to estimate these kinetic parameters.

The current study only evaluated the impact of AIF interpolation on kinetic parameter estimates for Patlak analysis of ^{68}Ga -PSMA-11 studies in prostate cancer. Nonetheless, the observed reduction in AIF peak and tail curve variability using the trained node weighting method demonstrates that proper AIF estimation enables improved downstream accuracy of kinetic parameter modeling. Although not specifically evaluated in the present study, it can be reasonably assumed that other graphical methods like Logan plot analysis and kinetic modeling would also benefit from enhanced AIF estimation. Trained methods such as node weighting may similarly enhance the performance of parametric modeling in broader dynamic PET applications. The relative advantage of the trained node weighting method will be dependent upon individual PET tracer pharmacokinetics and imaging study design. As such, one feasibility constraint of trained methods is the requirement for re-training when altering the image acquisition sequence or tracer. The reported AIF model parameterizes tracer differences in recirculation, RBC trapping, and RBC release, enabling the translation to other tracers with an upfront cost of validating the generated curves against pilot human data.

This study presents simulation data, and therefore the interpretation of the findings must be tempered by an understanding of the accompanying limitations. Foremost, all plasma function data was created from a parametric model which is not validated against image-derived AIFs or continuous arterial sampling data. Additionally, the models used for Patlak analysis did not account for image distortions or tracer decay corrections. Only a single scanner frame sequence was employed in this analysis, and although it was intended to represent a standard clinical PET study, any model-based interpolant methods would require retraining before application to new studies.

V. Conclusion

Input function interpolation method significantly impacts the accuracy and variability of kinetic rate parameters obtained through Patlak analysis. Model-based interpolation techniques surpass simple interpolation techniques in this simulated study of tracer kinetics. The results of this study indicate that the trained node weighting method provides a novel approach for AIF interpolation used for quantitative pharmacokinetic modeling in dynamic PET studies.

Acknowledgments

This work was supported by NIH R01CA202695.

VI. References

- [1]. Bertoldo A, Rizzo G, and Veronese M, "Deriving physiological information from PET images: from SUV to compartmental modelling," *Clin. Transl. Imaging*, vol. 2, no. 3, pp. 239–251, Jun. 2014, doi: 10.1007/s40336-014-0067-x.

- [2]. Alf MF, Wyss MT, Buck A, Weber B, Schibli R, and Krämer SD, “Quantification of Brain Glucose Metabolism by 18F-FDG PET with Real-Time Arterial and Image-Derived Input Function in Mice,” *J. Nucl. Med.*, vol. 54, no. 1, pp. 132–138, Jan. 2013, doi: 10.2967/jnumed.112.107474. [PubMed: 23160788]
- [3]. Carson R, Planeta-Wilson B, Mulnix T, and Frost J, “Image-based input functions from the carotid arteries with the HRRT,” *J. Nucl. Med.*, vol. 47, no. suppl 1, pp. 57P–57P, May 2006.
- [4]. Croteau E et al. , “Image-derived input function in dynamic human PET/CT: methodology and validation with 11C-acetate and 18F-fluorothioheptadecanoic acid in muscle and 18F-fluorodeoxyglucose in brain,” *Eur. J. Nucl. Med. Mol. Imaging*, vol. 37, no. 8, pp. 1539–1550, Aug. 2010, doi: 10.1007/s00259-010-1443-z. [PubMed: 20437239]
- [5]. Su Y et al. , “Quantitative hemodynamic PET imaging using image-derived arterial input function and a PET/MR hybrid scanner,” *J. Cereb. Blood Flow Metab.*, vol. 37, no. 4, pp. 1435–1446, Apr. 2017, doi: 10.1177/0271678X16656200. [PubMed: 27401805]
- [6]. Sundar LK et al. , “Towards quantitative [18F]FDG-PET/MRI of the brain: Automated MR-driven calculation of an image-derived input function for the non-invasive determination of cerebral glucose metabolic rates,” *J. Cereb. Blood Flow Metab.*, vol. 39, no. 8, pp. 1516–1530, Aug. 2019, doi: 10.1177/0271678X18776820. [PubMed: 29790820]
- [7]. Zanotti-Fregonara P et al. , “Image-Derived Input Function for Human Brain Using High Resolution PET Imaging with [11C](R)-rolipram and [11C]PBR28,” *PLOS ONE*, vol. 6, no. 2, p. e17056, Feb. 2011, doi: 10.1371/journal.pone.0017056. [PubMed: 21364880]
- [8]. Zanotti-Fregonara P et al. , “Population-based input function and image-derived input function for [11C](R)-rolipram PET imaging: Methodology, validation and application to the study of major depressive disorder,” *NeuroImage*, vol. 63, no. 3, pp. 1532–1541, Nov. 2012, doi: 10.1016/j.neuroimage.2012.08.007. [PubMed: 22906792]
- [9]. Naganawa M et al. , “Assessment of population-based input functions for Patlak imaging of whole body dynamic 18F-FDG PET,” *EJNMMI Phys.*, vol. 7, no. 1, p. 67, Nov. 2020, doi: 10.1186/s40658-020-00330-x. [PubMed: 33226522]
- [10]. Soret M, Bacharach SL, and Buvat I, “Partial-Volume Effect in PET Tumor Imaging,” *J. Nucl. Med.*, vol. 48, no. 6, pp. 932–945, Jun. 2007, doi: 10.2967/jnumed.106.035774. [PubMed: 17504879]
- [11]. Sari H et al. , “Estimation of an image derived input function with MR-defined carotid arteries in FDG-PET human studies using a novel partial volume correction method,” *J. Cereb. Blood Flow Metab.*, vol. 37, no. 4, pp. 1398–1409, Apr. 2017, doi: 10.1177/0271678X16656197. [PubMed: 27342321]
- [12]. Erlandsson K, Buvat I, Pretorius PH, Thomas BA, and Hutton BF, “A review of partial volume correction techniques for emission tomography and their applications in neurology, cardiology and oncology,” *Phys. Med. Biol.*, vol. 57, no. 21, pp. R119–R159, Oct. 2012, doi: 10.1088/0031-9155/57/21/R119. [PubMed: 23073343]
- [13]. Meyer M, Le-Bras L, Fernandez P, and Zanotti-Fregonara P, “Standardized Input Function for 18F-FDG PET Studies in Mice: A Cautionary Study,” *PLOS ONE*, vol. 12, no. 1, p. e0168667, Jan. 2017, doi: 10.1371/journal.pone.0168667. [PubMed: 28125579]
- [14]. Feng D and Wang X, “A computer simulation study on the effects of input function measurement noise in tracer kinetic modeling with positron emission tomography (PET),” *Comput. Biol. Med.*, vol. 23, no. 1, pp. 57–68, Jan. 1993, doi: 10.1016/0010-4825(93)90108-D. [PubMed: 8467639]
- [15]. Huesman RH and Mazoyer BM, “Kinetic data analysis with a noisy input function,” *Phys. Med. Biol.*, vol. 32, no. 12, pp. 1569–1579, Dec. 1987, doi: 10.1088/0031-9155/32/12/004. [PubMed: 3501592]
- [16]. Feng D, Huang S-C, and Wang X, “Models for computer simulation studies of input functions for tracer kinetic modeling with positron emission tomography,” *Int. J. Biomed. Comput.*, vol. 32, no. 2, pp. 95–110, Mar. 1993, doi: 10.1016/0020-7101(93)90049-C. [PubMed: 8449593]
- [17]. Chen K, Huang S-C, and Feng D, “New estimation methods that directly use the time accumulated counts in the input function in quantitative dynamic PET studies,” *Phys. Med. Biol.*, vol. 39, no. 11, pp. 2073–2090, Nov. 1994, doi: 10.1088/0031-9155/39/11/017. [PubMed: 15560012]

- [18]. Patlak CS, Blasberg RG, and Fenstermacher JD, “Graphical valuation of Blood-to-Brain Transfer Constants from Multiple-Time Uptake Data,” *J. Cereb. Blood Flow Metab*, vol. 3, no. 1, pp. 1–7, Mar. 1983, doi: 10.1038/jcbfm.1983.1. [PubMed: 6822610]
- [19]. Hope TA, Goodman JZ, Allen IE, Calais J, Fendler WP, and Carroll PR, “Meta-analysis of 68Ga-PSMA-11 PET Accuracy for the Detection of Prostate Cancer Validated by Histopathology,” *J. Nucl. Med*, vol. 60, no. 6, pp. 786–793, Jun. 2019, doi: 10.2967/jnumed.118.219501. [PubMed: 30530831]
- [20]. Kimura S et al. , “Performance of [68Ga] Ga-PSMA 11 PET for detecting prostate cancer in the lymph nodes before salvage lymph node dissection: a systematic review and meta-analysis,” *Prostate Cancer Prostatic Dis*, vol. 23, no. 1, Art. no. 1, Mar. 2020, doi: 10.1038/s41391-019-0156-z.
- [21]. Calais J et al. , “Impact of 68Ga-PSMA-11 PET/CT on the Management of Prostate Cancer Patients with Biochemical Recurrence,” *J. Nucl. Med*, vol. 59, no. 3, pp. 434–441, Mar. 2018, doi: 10.2967/jnumed.117.202945. [PubMed: 29242398]
- [22]. Fendler WP et al. , “68Ga-PSMA PET/CT: Joint EANM and SNMMI procedure guideline for prostate cancer imaging: version 1.0,” *Eur. J. Nucl. Med. Mol. Imaging*, vol. 44, no. 6, pp. 1014–1024, Jun. 2017, doi: 10.1007/s00259-017-3670-z. [PubMed: 28283702]
- [23]. Fourquet A et al. , “68Ga-PSMA-11 PET/CT in restaging castration-resistant nonmetastatic prostate cancer: detection rate, impact on patients’ disease management and adequacy of impact,” *Sci. Rep*, vol. 10, no. 1, Art. no. 1, Feb. 2020, doi: 10.1038/s41598-020-58975-8.
- [24]. Kawada T et al. , “Diagnostic Performance of Prostate-specific Membrane Antigen Positron Emission Tomography–targeted biopsy for Detection of Clinically Significant Prostate Cancer: A Systematic Review and Meta-analysis,” *Eur. Urol. Oncol*, vol. 5, no. 4, pp. 390–400, Aug. 2022, doi: 10.1016/j.euo.2022.04.006. [PubMed: 35715320]
- [25]. Woo S et al. , “Prostate-specific membrane antigen positron emission tomography (PSMA-PET) for local staging of prostate cancer: a systematic review and meta-analysis,” *Eur. J. Hybrid Imaging*, vol. 4, no. 1, p. 16, Sep. 2020, doi: 10.1186/s41824-020-00085-9. [PubMed: 34191215]
- [26]. Ringheim A et al. , “Kinetic modeling of 68Ga-PSMA-11 and validation of simplified methods for quantification in primary prostate cancer patients,” *EJNMMI Res*, vol. 10, no. 1, p. 12, Feb. 2020, doi: 10.1186/s13550-020-0594-6. [PubMed: 32140850]
- [27]. Strauss DS, Sachpekidis C, Kopka K, Pan L, Haberkorn U, and Dimitrakopoulou-Strauss A, “Pharmacokinetic studies of [68 Ga]Ga-PSMA-11 in patients with biochemical recurrence of prostate cancer: detection, differences in temporal distribution and kinetic modelling by tissue type,” *Eur. J. Nucl. Med. Mol. Imaging*, vol. 48, no. 13, pp. 4472–4482, Dec. 2021, doi: 10.1007/s00259-021-05420-1. [PubMed: 34110436]
- [28]. Begum NJ, Glattig G, Wester H-J, Eiber M, Beer AJ, and Kletting P, “The effect of ligand amount, affinity and internalization on PSMA-targeted imaging and therapy: A simulation study using a PBPK model,” *Sci. Rep*, vol. 9, no. 1, Art. no. 1, Dec. 2019, doi: 10.1038/s41598-019-56603-8.
- [29]. Patel HN et al. , “Normal Values of Cardiac Output and Stroke Volume According to Measurement Technique, Age, Sex, and Ethnicity: Results of the World Alliance of Societies of Echocardiography Study,” *J. Am. Soc. Echocardiogr. Off. Publ. Am. Soc. Echocardiogr*, vol. 34, no. 10, pp. 1077–1085.e1, Oct. 2021, doi: 10.1016/j.echo.2021.05.012.
- [30]. Lang RM et al. , “Recommendations for Cardiac Chamber Quantification by Echocardiography in Adults: An Update from the American Society of Echocardiography and the European Association of Cardiovascular Imaging,” *Eur. Heart J. - Cardiovasc. Imaging*, vol. 16, no. 3, pp. 233–271, Mar. 2015, doi: 10.1093/ehjci/jev014. [PubMed: 25712077]
- [31]. Billett HH, “Hemoglobin and Hematocrit,” in *Clinical Methods: The History, Physical, and Laboratory Examinations*, Walker HK, Hall WD, and Hurst JW, Eds., 3rd ed. Boston: Butterworths, 1990. Accessed: Sep. 23, 2023. [Online]. Available: <http://www.ncbi.nlm.nih.gov/books/NBK259/>
- [32]. Fooladi M, Rezaei S, Aghahosseini F, Salehi Y, Kasraie N, and Sheikhzadeh P, “Impact of Region-of-Interest Delineation on Stability and Reproducibility of Liver SNR Measurements in 68 Ga-PSMA PET/CT,” *World J. Nucl. Med*, vol. 22, no. 2, pp. 124–129, May 2023, doi: 10.1055/s-0043-1768446. [PubMed: 37223627]

- [33]. Franiel T, L demann L, Rudolph B, Lutterbeck E, Hamm B, and Beyersdorff D, “Differentiation of Prostate Cancer From Normal Prostate Tissue: Role of Hotspots in Pharmacokinetic MRI and Histologic Evaluation,” *Am. J. Roentgenol*, vol. 194, no. 3, pp. 675–681, Mar. 2010, doi: 10.2214/AJR.09.3233. [PubMed: 20173144]
- [34]. Logan J et al. , “Strategy for the Formation of Parametric Images under Conditions of Low Injected Radioactivity Applied to PET Studies with the Irreversible Monoamine Oxidase a Tracers [11C]Clorgyline and Deuterium-Substituted [11C]Clorgyline,” *J. Cereb. Blood Flow Metab*, vol. 22, no. 11, pp. 1367–1376, Nov. 2002, doi: 10.1097/01.WCB.0000040947.67415.e1. [PubMed: 12439294]
- [35]. Paszke A et al. , “PyTorch: An Imperative Style, High-Performance Deep Learning Library.” *arXiv*, Dec. 03, 2019. Accessed: Nov. 23, 2022. [Online]. Available: <http://arxiv.org/abs/1912.01703>
- [36]. He K, Zhang X, Ren S, and Sun J, “Deep Residual Learning for Image Recognition.” *arXiv*, Dec. 10, 2015. Accessed: Sep. 26, 2022. [Online]. Available: <http://arxiv.org/abs/1512.03385>

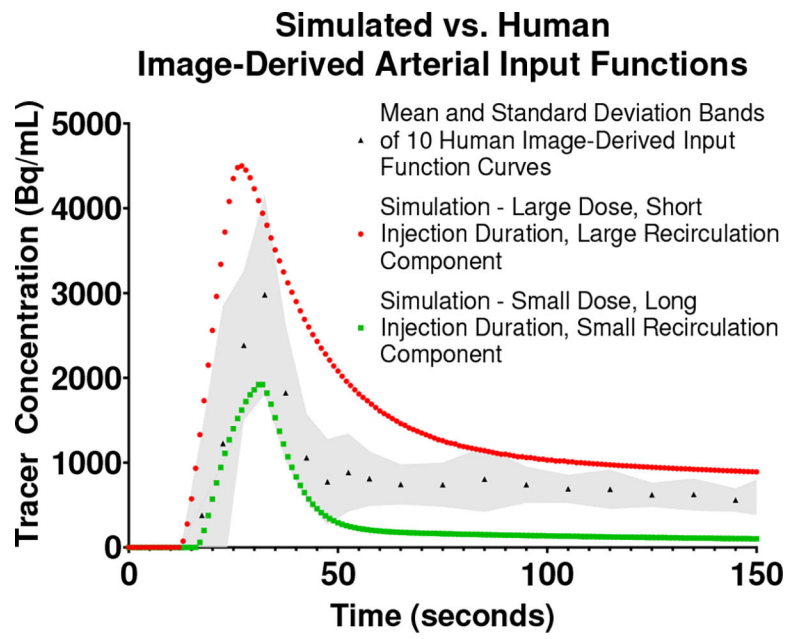


Figure 1: Overlay of the mean and standard deviation of 10 human (grey) and 2 simulated image-derived PSMA-11 AIFs. Human-derived datasets were acquired as part of an ongoing clinical research trial [NCT04936334](#).

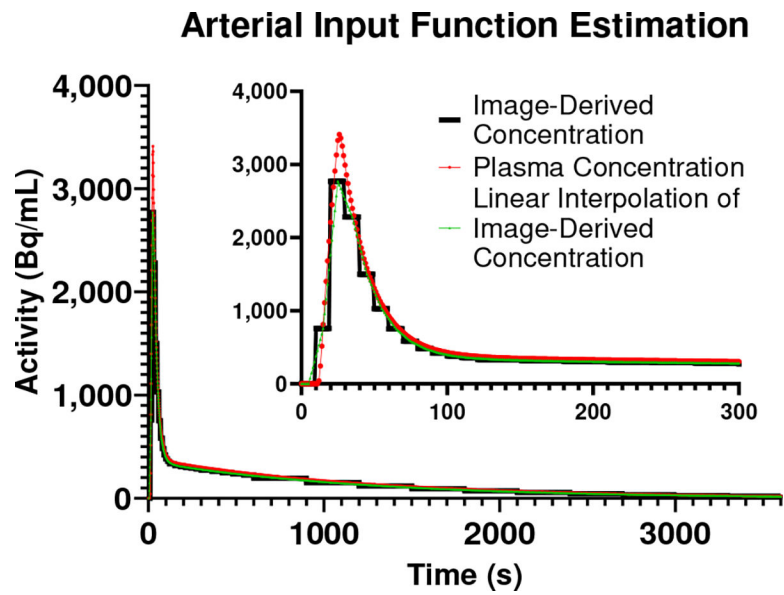


Figure 2:

A sample simulated AIF, displayed with an inset graph of the first 300 seconds of the simulated TAC. The red curve represents the simulated plasma function $C_{plasma}(t)$, which is binned into an image-derived blood TAC, $C_{blood}(t)$. The green curve is a linear interpolation of $C_{blood}(t)$ intended to approximate $C_{plasma}(t)$.

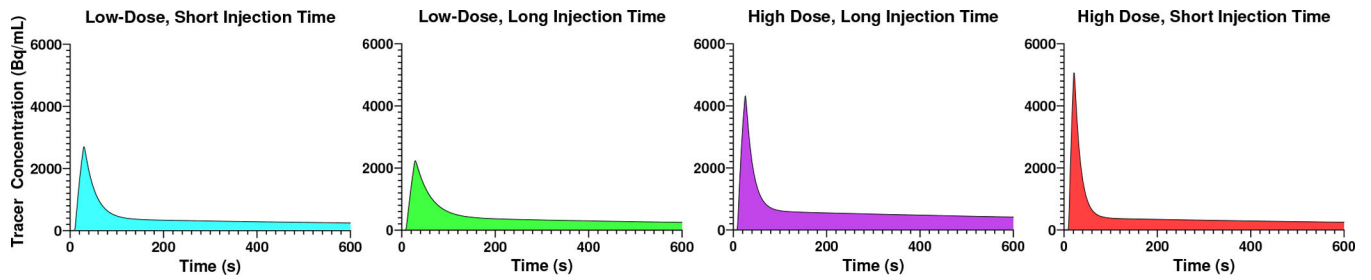


Figure 3:

Demonstration of the distribution of modeled plasma input function curves. Shown are the first 600 seconds of four simulated input function curves drawn from the study simulation. Light blue and light green show an input function within the bottom 5% of simulated injected doses and with a minimum or maximum injection time, respectively. Red and purple show an input function within the top 5% of simulated injected doses and with a minimum or maximum injection time, respectively. Curves are displayed without noise.

Input Function Peak - Residual Mean and Standard Deviation

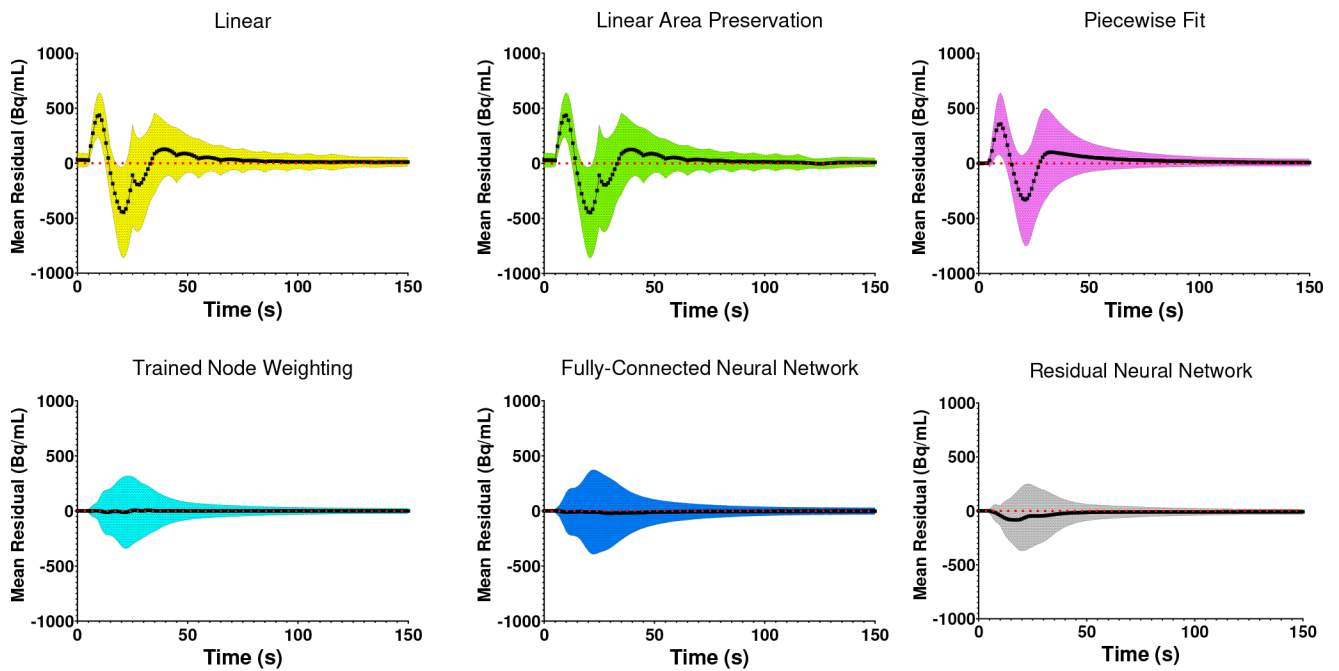


Figure 4:

Interpolation method performance during the bolus phase (first 150 seconds) of the AIF TAC. Each plot displays the mean temporal bias (black) and residual standard deviation (root mean squared error, denoted by color bands) relative to a zero-residual target line (red dashed line). The linear and linear area preservation methods are nearly identical, except for slight differences at the frame duration transition that occurs at $t=120$ seconds.

Input Function Tail - Residual Mean and Standard Deviation

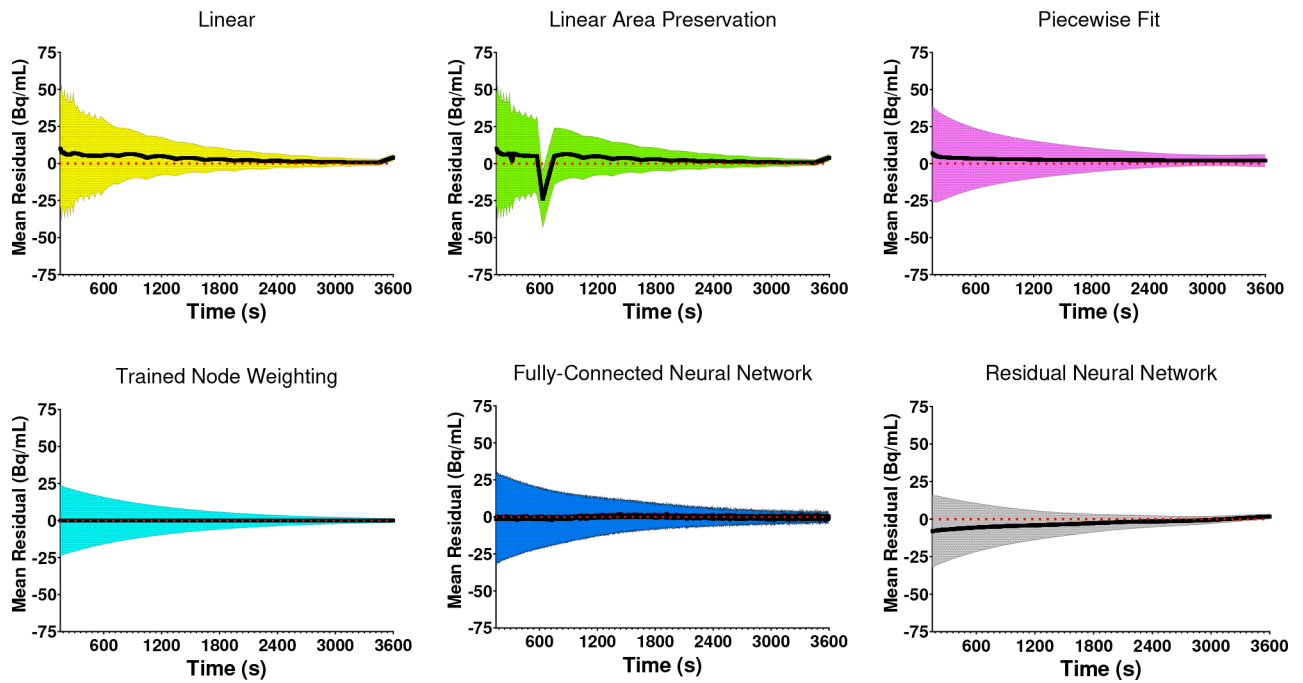


Figure 5: Interpolation method performance after the bolus phase (final 3450 seconds) of the AIF TAC. Each plot displays the mean temporal bias (black) and residual standard deviation (root mean squared error, denoted by color bands) relative to a zero-residual target line (red dashed line). The spikes in the linear area preservation method bias occur at frame sequence transition timepoints at $t=300$ and $t=600$ seconds.

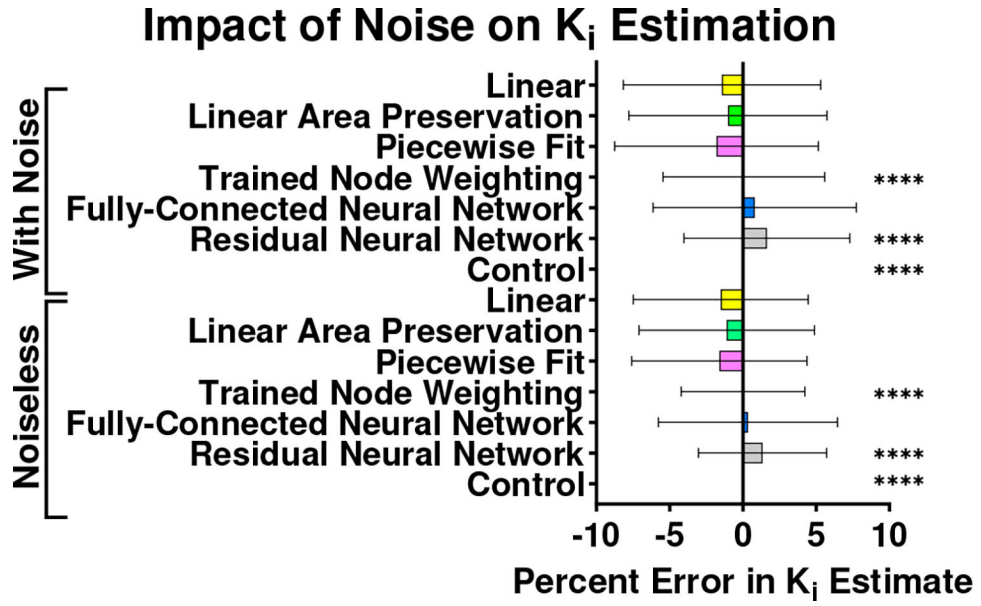


Figure 6: Mean estimation error and standard deviation for the net tracer influx rate, K_i , for each interpolation method. Results are shown with and without noise within a random, uniform SNR range of 4–10. The noiseless comparisons demonstrate the K_i estimation errors and variability which are attributable to systematic (non-noise) causes. Significance indicates a reduction in K_i estimation variability relative to linear interpolation, using a one-sided F-test for variance, corrected for multiple comparisons using the Bonferroni method. (****) indicates $p < 0.0001$.

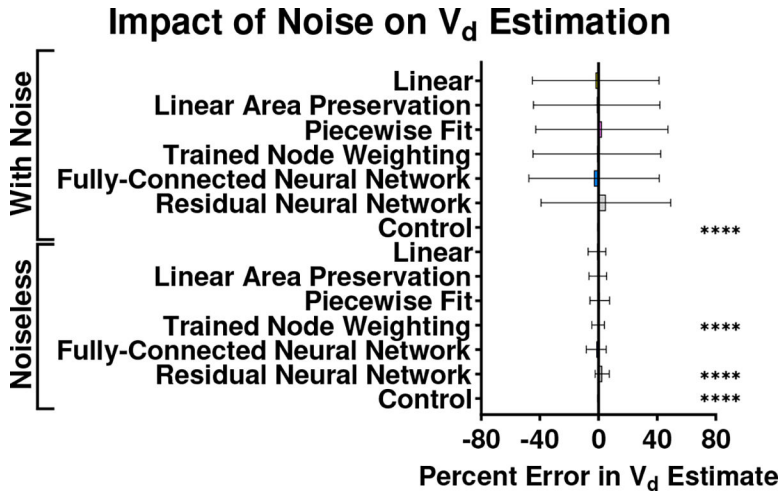


Figure 7: Mean estimation error and standard deviation for the tracer distribution volume, V_d , for each interpolation method. Results are shown with and without noise within a random, uniform SNR range of 4–10. The noiseless comparisons demonstrate the V_d estimation errors and variability which are attributable to systematic (non-noise) causes. Significance indicates a reduction in V_d estimation variability relative to linear interpolation, using a one-sided F-test for variance, corrected for multiple comparisons using the Bonferroni method. (****) indicates $p < 0.0001$

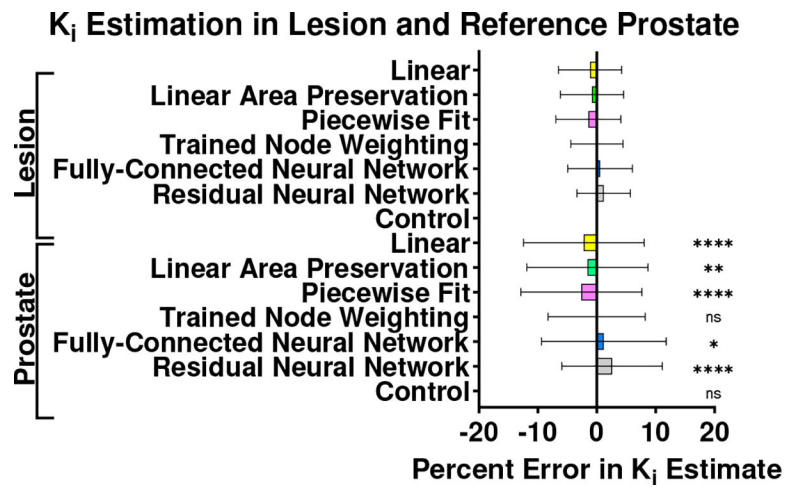


Figure 8: Mean estimation error and standard deviation for the net tracer influx rate, K_i , for each interpolation method. Results are grouped by lesion (defined as reference $K_i > 0.024\text{min}^{-1}$, $N = 1350$) or normal prostate (defined as reference $K_i < 0.022\text{min}^{-1}$, $N = 3276$). Significance indicates a difference in pooled bias between normal prostate and lesion K_i estimates. Significance levels are * $p < 0.05$, ** $p < 0.01$, *** $p < 0.001$, **** $p < 0.0001$

Table 1:

Definitions and Constraints on Parameter Values. EMP = estimated empirically

Parameter	Definition	Normally Distributed (μ, σ, min, max)	Uniformly Distributed (min, max)	Ref.
D	Injected Dose (MBq)	-	(90, 110)	EMP
T_{inject}	Injected Dose Duration (s)	-	(10, 20)	EMP
T_{delay}	Bolus Arrival Time Delay (s)	(8, 2, 0, 30)	-	EMP
CO	Cardiac Output (L/min)	(4.8, 0.3, 3, 7)	-	[29]
LVEDV	Left-ventricular End-Diastolic Volume (mL)	(107, 10, 60, 150)	-	[30]
V	Vein to Pulmonary Artery Rate Constant (s ⁻¹)	(0.05, 0.0083, 0.00001, 1)	-	EMP
H	Left Ventricular Rate Constant (s ⁻¹) $H = \frac{CO}{LVEDV} \left(\frac{1000}{60} \right)$	-	-	-
RF	Tracer Recirculation Fraction	(0.005, 0.0005, 0.00001, 1)	-	EMP
RR	Recirculation Rate Constant (s ⁻¹)	(0.00083, 0.000083, 0.00001, 1)	-	EMP
RT_{delay}	Recirculation Time Delay (s)	(45, 10, 0, 75)	-	EMP
Hct	Hematocrit Percentage	(0.42, 0.04, 0.2, 0.7)	-	[31]
R₁	RBC Trapping Rate Constant (s ⁻¹)	(1, 0.1, 0.00001, 5)	-	EMP
R₂	RBC Release Rate Constant (s ⁻¹)	(1, 0.1, 0.00001, 5)	-	EMP
SNR	Signal-to-Noise Ratio	-	(4, 10)	EMP, supported by [32]
F_{BV}	Fractional Blood Volume	-	(0, 0.05)	[33]
K₁	Kinetic Rate Constant $\left(\frac{mL_{blood}}{mL_{tissue} \cdot min} \right)$	(0.112, 0.07, 0.00001, 0.5)	-	[26]
k₂	Kinetic Rate Constant (min ⁻¹)	(0.258, 0.05, 0.00001, 0.5)	-	[26]
k₃	Kinetic Rate Constant (min ⁻¹)	(0.074, 0.03, 0.00001, 0.5)	-	[26]

Table II:

Statistical results comparing the estimated area under the plasma arterial input function curve ($C_p(t)$) through each interpolation method to the noiseless control arterial input function. Only the trained node weighting and fully-connected neural network interpolation methods did not significantly differ in the calculated total area under the curve, and only the trained node weighting method additionally preserved area underneath the curve peak. Each q-statistic is evaluated with 4,999 degrees of freedom.

Preservation of Total Area Under the Curve						
Dunnnett's multiple comparisons test	Mean Difference	SE	q-statistic	Summary Significance	Adjusted P-Value	
Control vs. Linear	-12830	612.8	20.94	****	<0.0001	
Control vs. Linear Area Preservation	-9874	610.1	16.18	****	<0.0001	
Control vs. Piecewise Fit	-12557	614.9	20.42	****	<0.0001	
Control vs. Trained Node Weighting	190.8	446.9	0.4268	ns	0.9958	
Control vs. Fully-Connected Neural Network	1369	602.9	2.271	ns	0.1053	
Control vs. Residual Neural Network	12173	449.7	27.07	****	<0.0001	
Preservation of Area Under the Peak of the Curve (first 150 seconds)						
Dunnnett's multiple comparisons test	Mean Difference	SE	q-statistic	Summary Significance	Adjusted P-Value	
Control vs. Linear	-2081	165.0	12.61	****	<0.0001	
Control vs. Linear Area Preservation	-1918	164.7	11.65	****	<0.0001	
Control vs. Piecewise Fit	-3356	167.5	20.03	****	<0.0001	
Control vs. Trained Node Weighting	61.19	93.65	0.6534	ns	0.9694	
Control vs. Fully-Connected Neural Network	891.8	154.1	5.786	****	<0.0001	
Control vs. Residual Neural Network	2762	93.11	29.66	****	<0.0001	

(****) indicates $p < 0.0001$. (ns) indicates that the result is not statistically significant.